Journal of Geophysical Research: Planets

The vertical distribution of Martian aerosol particle size

Scott D. Guzewich[1], Michael D. Smith[1], and Michael J. Wolff[2]

[1]NASA Goddard Spaceflight Center, Greenbelt, Maryland, USA, [2]Space Science Institute, Boulder, Colorado, USA

Abstract Using approximately 410 limb-viewing observations from the Compact Reconnaissance Imaging Spectrometer for Mars (CRISM), we retrieve the vertical distribution of Martian dust and water ice aerosol particle sizes. We find that dust particles have an effective radius of 1.0 μm over much of the atmospheric column below 40 km throughout the Martian year. This includes the detached tropical dust layers detected in previous studies. Little to no variation with height is seen in dust particle size. Water ice clouds within the aphelion cloud belt exhibit a strong sorting of particle size with height, however, and the effective radii range from >3 μm below 20 km to near 1.0 μm at 40 km altitude. Conversely, water ice clouds in the seasonal polar hoods show a near-uniform particle size with an effective radius of approximately 1.5 μm throughout the atmospheric column.

1. Introduction

The canonical size distributions assumed for Martian aerosols have most often been an effective radius of 1.5 μm for dust and 2.0 μm for water ice [e.g., *Smith et al.*, 2013]. These values have been corroborated by several investigations using multiple instruments [e.g., *Toon et al.*, 1977; *Clancy et al.*, 1995; *Pollack et al.*, 1995; *Wolff and Clancy*, 2003; *Wolff et al.*, 2006]. However, those canonical values have most often been best-fit values to the column-integrated dust or water ice observations and are thus biased to the lowest altitudes where aerosol opacity is highest. Indeed, it is well known that aerosol particle size is not constant in time or space, and variations in particle size have been observed with both smaller [*Rannou et al.*, 2006; *Määttänen et al.*, 2013] and larger particle sizes [*Clancy et al.*, 2003, 2010] than the canonical column-averaged and seasonally averaged values.

It is also expected that aerosol particle size will be a function of height above the surface. The vertical distribution of aerosol particle size has been examined using Mars Express/SPICAM observations [*Fedorova et al.*, 2009, 2014; *Määttänen et al.*, 2013]. The size distribution of Martian aerosols and its variation with height affects the interaction of the aerosols with solar visible and infrared radiation and thus influences the Martian climate. Current general circulation models (GCMs) with active dust and water cycles are attempting to tune these parameters to fit the observations [e.g., *Kahre et al.*, 2006; *Wilson and Guzewich*, 2014; *Madeleine et al.*, 2012]. This tuning of aerosol parameters so the GCM simulation matches other observations (i.e., temperature) often results in model aerosol properties poorly matching observed aerosol properties. We expect our results will inform the way that aerosols are treated in the radiative transfer subroutines of atmospheric modeling by firmly constraining aerosol particle size throughout the atmospheric column and provide constraints for models that actively lift dust and produce water ice particles through microphysical parameterizations.

The use of limb-viewing geometry to examine the Martian atmosphere has revealed the previously unanticipated presence of discrete layers of dust, water ice, and carbon dioxide clouds [*Heavens et al.*, 2011; *Guzewich et al.*, 2013; *Määttänen et al.*, 2013; *Montmessin et al.*, 2006]. A layer of enhanced dust mixing ratio at 20–30 km above the Martian tropics has been identified in Mars Climate Sounder (MCS) [*Heavens et al.*, 2011] and Thermal Emission Spectrometer (TES) observations [*Guzewich et al.*, 2013]. *Määttänen et al.* [2013] found discrete detached aerosol layers in approximately half of all Mars Express/SPICAM profiles examined with varying composition. MCS observations further elucidated the greater vertical extent of tropical water ice clouds than what general circulation models and previous observational constraints had determined [*Heavens et al.*, 2010].

Small dust particle size has been postulated as a possible factor in maintaining these high-altitude discrete layers over long time periods as observed [*Guzewich et al.*, 2013]. Small dust particles have a slower fall speed and thus could be resupplied at less frequent intervals while providing more opportunity for deposition of
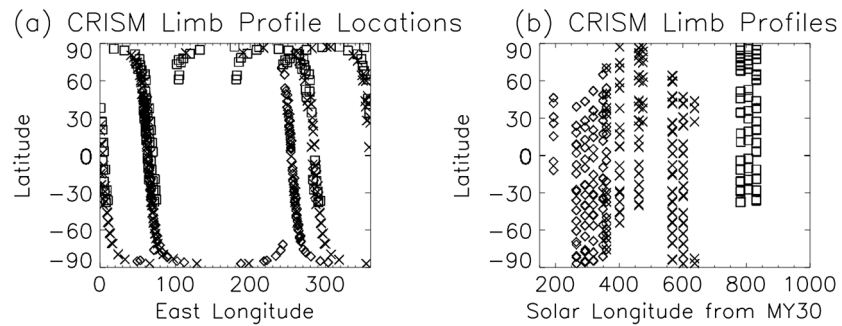
Figure 1. (a) Locations of CRISM limb-viewing geometry observations included in this study. (b) The same CRISM observations displayed by date and latitude. Diamonds correspond to MY 30, crosses to MY 31, and squares to MY 32.

water vapor and the formation of water ice clouds. This work addresses whether dust particle size is an explanatory factor in the maintenance of high altitude dust layers.

During the extended mission of the Mars Reconnaissance Orbiter (MRO), the Compact Reconnaissance Imaging Spectrometer for Mars (CRISM) [*Murchie et al.*, 2007] has conducted periodic limb-viewing geometry observations of the Martian atmosphere [*Smith et al.*, 2013]. This has enabled the retrieval of the vertical distribution of dust and water ice aerosol particle size. This paper presents these results and their implications. Section 2 describes the CRISM instrument, data collection, and retrieval algorithm. Section 3 discusses the retrieved aerosol particle sizes and their implications, while we summarize the observations and conclusions in section 4.

2. CRISM Instrument, Data, and Retrieval Methodology

2.1. CRISM Instrument and Data

CRISM is a hyperspectral visible and near-infrared imaging spectrometer onboard MRO that was primarily designed to examine surface mineralogy and geochemistry [*Murchie et al.*, 2007]. CRISM has additional atmospheric science capabilities involving atmospheric aerosols [e.g., *Wolff et al.*, 2009] and gas species [e.g., *Smith*, 2004; *Toigo et al.*, 2013]. The spectral range of CRISM is from 362 to 3920 nm with a spectral resolution of 10–15 nm [*Murchie et al.*, 2007]. CRISM is primarily a nadir-viewing instrument, though it is mounted on a gimbal to allow off-nadir observations. In fact, the instrument was designed to scan over a sufficient angular range to allow for construction of emission phase function sequences (EPF) [e.g., *Clancy and Lee*, 1991].

During a CRISM limb-viewing observation, the entire MRO spacecraft is pitched to allow CRISM to use its gimbal and scan upward and downward across the limb of the planet from the surface to above 120 km altitude. During a CRISM limb observation sequence, called a "limb set," the limb is scanned continuously, creating a profile approximately every 10° of latitude from pole to pole. Two or three longitudes are sampled, typically over Tharsis and Hellas/Syrtis Major (see Figure 1). Twenty-one limb sets covering a range of seasons and aerosol loading conditions have been obtained to date. Scattered sunlight from aerosols is typically observed by CRISM between the surface and about 50–60 km altitude in CRISM limb observations. The spatial resolution of each CRISM pixel is approximately 800 m at the limb tangent point after 10×10 pixel averaging on board the spacecraft. As part of the retrieval algorithm, we perform further spatial averaging to improve signal to noise. The central 40 pixels of each CRISM hyperspectral image are averaged parallel to the limb, and a running average of 3 pixels perpendicular to the limb is conducted. The resulting vertical sampling is approximately 3–4 km.

CRISM limb-viewing observations are available on the Planetary Data System and have the prefix of "LMB." Table 1 lists all CRISM limb sets by date. For this retrieval, we use only those observations with incidence angle less than 85°. All observations used for this study occur at approximately 15:00 local time, and the spatial locations (latitude, longitude, and solar longitude) are presented in Figure 1.

2.2. Retrieval Algorithm

The retrieval algorithm used in this study is an extension of that used by *Smith et al.* [2013] for their retrieval of vertical profiles of dust and water ice aerosol abundance using CRISM limb-geometry observations. The

Table 1. Dates of CRISM Limb Sets

Earth Date	Mars Date and Season
10–11 July 2009	MY 29, $L_s = 301°$
10–11 February 2010	MY 30, $L_s = 50°$
7 April 2010	MY 30, $L_s = 74°$
28–29 April 2010	MY 30, $L_s = 84°$
26 May 2010	MY 30, $L_s = 96°$
22–24 August 2010	MY 30, $L_s = 137°$
17 October 2010	MY 30, $L_s = 166°$
5–-6 December 2010	MY 30, $L_s = 193°$
31 March to 1 April 2011	MY 30, $L_s = 265°$
14–15 May 2011	MY 30, $L_s = 319°$
28 June 2011	MY 30, $L_s = 349°$
22–23 August 2011	MY 31, $L_s = 0°$
13 September 2011	MY 31, $L_s = 41°$
10–11 December 2011	MY 31, $L_s = 41°$
24–26 April 2012	MY 31, $L_s = 102°$
22–24 May 2012	MY 31, $L_s = 114°$
14–16 November 2012	MY 31, $L_s = 207°$
8–10 January 2013	MY 31, $L_s = 241°$
5–7 March 2013	MY 31, $L_s = 277°$
11–13 December 2013	MY 32, $L_s = 61°$
5–6 February 2014	MY 32, $L_s = 85°$
1–3 April 2014	MY 32, $L_s = 111°$

effective aerosol particle size and abundance (expressed in the form of a mixing ratio) are determined by radiative transfer modeling of the CRISM spectra with retrieved parameters adjusted to produce the closest match between the observed and calculated spectrum. The retrieval algorithm minimizes the chi-square difference between the observed radiance and the radiance computed by a forward model using the Marquardt-Levenberg algorithm [*Press et al.*, 1992].

The retrieval uses 12 wavelengths in the near-infrared portion of the CRISM spectrum: 1283.3, 1513.2, 1783, 2218.6, 2549.3, 2635.1, 2906.2, 2979.1, 3105, 3304.1, 3503.5, and 3703.3 nm (Figure 2). These wavelengths were selected to maximize the sensitivity to aerosol particle size (Figures 4 and 5), avoid strong gas absorption bands, and keep the number of channels to a reasonably small number (for computational efficiency). The sample spans the spectral range from 1300 to 3700 nm with several wavelengths clustered near the 2800 nm water ice absorption feature. At these wavelengths (i.e., nonthermal), the light observed by CRISM comes from scattering by atmospheric aerosols and so multiple scattering is explicit using the discrete ordinates method [e.g., *Goody and Yung*, 1989; *Thomas and Stamnes*, 1999]. The limb-viewing geometry necessitates an explicit treatment of the inherent spherical geometry. For the sake of computational efficiency, we employ a "pseudo-spherical" approximation that has been well tested against an "exact" fully spherical Monte Carlo radiative transfer code for the geometries represented by the CRISM observations. This approach has been found to be accurate to within a few percent while nearly 2 orders of magnitude faster computationally [*Wolff et al.*, 2006; *Smith et al.*, 2013]. Further details on the particular implementation of pseudo-spherical approximation and its validation are presented in *Smith et al.* [2013].

The retrieved quantities are the effective particle size and the abundances (expressed in terms of a mixing ratio) for both dust and water ice aerosols at 18 vertical levels equally spaced every 0.4 pressure scale heights between 0.2 and 6.6 scale heights above the surface. Also retrieved is the effective Lambert surface albedo at each of the 12 wavelengths used in the retrieval. This results in a total of 84 free parameters.
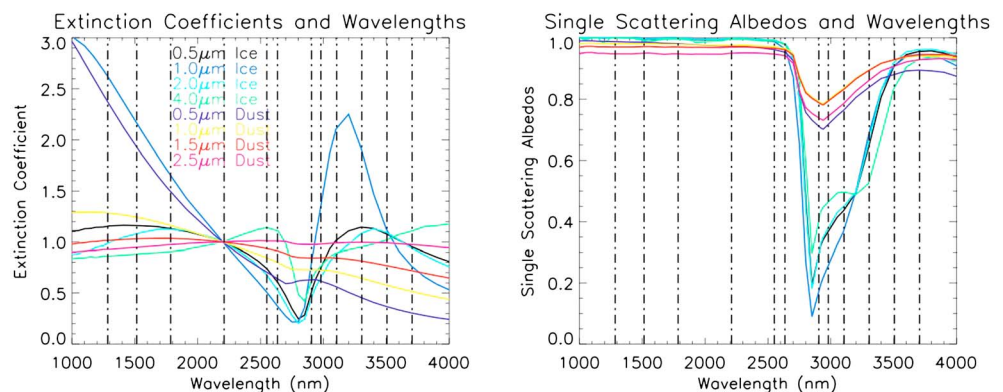
Figure 2. (left) Extinction coefficients and (right) single scattering albedos as a function of wavelength for the eight representative particle size distributions (solid color lines). The wavelengths used in the retrieval algorithm are shown as dashed-dotted lines.
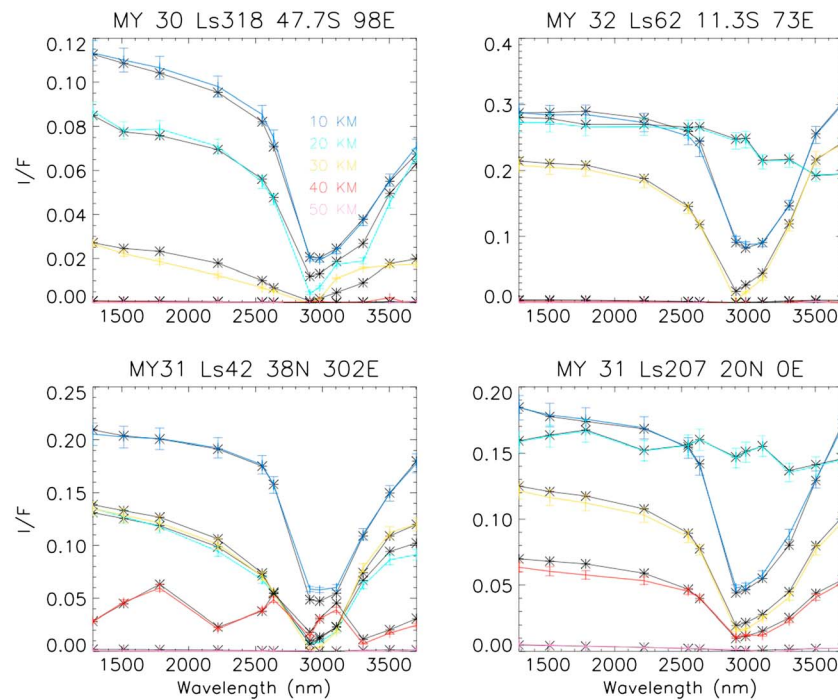
Figure 3. Four example fits of CRISM radiance observations at the indicated times and locations in varying aerosol-loading conditions. Colored lines correspond to the observed radiance at the indicated tangent heights with 5% error bars, following *Wolff et al.* [2009]. Black lines are the calculated radiances at each tangent height.

The aerosol size distribution for both dust and water ice aerosol is prescribed using the modified gamma distribution of *Deirmendjian* [1964]. The retrieved size information for both dust and water ice aerosols is the effective radii, r_{eff}; the effective variance is held fixed and assumed to be 0.3 for dust and 0.1 for water ice [*Wolff et al.*, 2009; *Smith et al.*, 2013]. There is a degeneracy between the retrieval of effective radius and effective variance, hence fixing the effective variance allows us to retrieve effective radii directly. Additionally, there is little sensitivity to variations of effective variance over reasonable values (not shown). Dust refractive indices are taken from *Wolff et al.* [2009] and assumed to be cylindrical with a diameter-to-length aspect ratio of unity. Its radiative properties are calculated using the T-matrix formalism [*Mishchenko et al.*, 2000]. Water ice aerosols are assumed to be spherical, and the scattering phase function is computed using Mie theory [*Warren*, 1984; *Wiscombe*, 1996].

The computed extinction coefficients and single scattering albedos for dust and water ice aerosol are shown in Figure 2 for a range of effective radii reported in previous studies, along with the locations of the 12 wavelengths used in the retrieval. The extinction coefficients are normalized to be unity at a reference wavelength of 2200 nm, and thus, retrieved mixing ratios (in units of $\Delta\tau$/mb) are referenced to the optical depth at that wavelength and represent "extinction mixing ratios."

The retrieval is performed in two steps. First, the effective radii for both dust and water ice aerosols at all vertical levels are held fixed at a nominal value, and only the aerosol mixing ratio (and Lambert surface albedo) is retrieved. A second step repeats the retrieval, fitting for both aerosol mixing ratios and effective radii at all levels. The full retrieval including all 84 free parameters is computationally expensive, and this simplified first step provides an accurate first guess for the second step, reducing the number of iterations required for convergence. The algorithm only attempts to fit aerosol particle size at a given altitude level if the mixing ratio of that aerosol is ≥0.09 $\Delta\tau$/mb at that level. We compared retrieved aerosol mixing ratio between our retrieval algorithm and that of *Smith et al.* [2013] and find trivial differences between the two.

Figure 3 shows four examples of the fit between the observed radiance (colored lines) at five tangent heights compared to the corresponding calculated radiance (black lines) with varying aerosol-loading conditions. The overall variation of brightness (I/F) as a function of height above the surface is primarily related to the vertical distribution of aerosol mixing ratio ($\Delta\tau$/mb). The differentiation between dust and water ice aerosol,
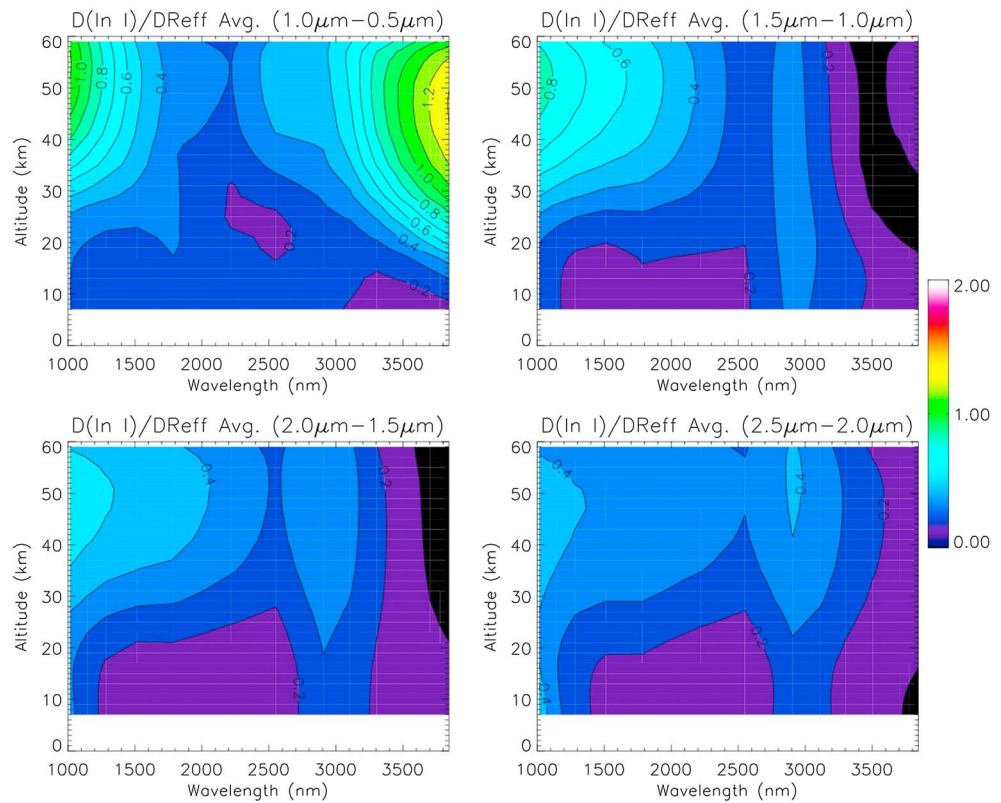
Figure 4. $\frac{d\,(\ln I)}{dr_{eff}}$ of CRISM observations over the indicated intervals in dust effective radius in units of μm^{-1} as a function of wavelength and altitude. Larger numbers indicate greater sensitivity to dust effective radius.

and the determination of particle size is primarily revealed through the wavelength dependence of the brightness at each altitude.

2.2.1. Uncertainties

Uncertainties in this work arise from a variety of assumptions and numerical simplifications in the retrieval algorithm including the pseudo-spherical assumption, the choice of constant effective variance, and the initial guess of particle size used in the retrieval algorithm. Additional instrumental errors may propagate into the solution, although as described by *Smith et al.* [2013], spatial averaging of pixels reduces this source of uncertainty greatly.

We tested three sources of uncertainties to quantify their impact to retrieved aerosol particle effective radius. First, we tested sensitivity to the initial guess of aerosol effective radius. This initial guess of effective radius is used in the first step of the retrieval that does not include fitting for particle effective radius. We examined several initial values of dust and water ice aerosol effective radius (e.g., 0.5, 1.0, 1.5, and 2.5 μm for dust) for a number of CRISM limb-viewing geometry observations to determine how this influenced the final retrieved aerosol effective radius found in the second step of the retrieval. As stated in section 2.2, we find that the CRISM observations are more sensitive to smaller particles, with decreasing sensitivity to dust particle size distributions with effective radius greater than 1.5 μm (Figure 4). For dust particles smaller than 1.5 μm, the initial guess of particle size resulted in a change of ±0.1 μm. For larger dust particles, this variability increased to ±0.25 μm. The retrieval algorithm is more sensitive to differentiating ice effective radii compared to dust effective radii (compare Figures 4 and 5), and we estimate the uncertainty caused by the initial guess of ice aerosol effective radius to be ±0.1 μm.

The second source of uncertainty we examined is the uncorrelated noise that is attributable to instrument noise that is uncorrelated versus wavelength and a combination of the other uncertainties in the retrieval algorithm such as the pixel averaging, constant aerosol particle effective variance, number of streams, and number of vertical levels (additional details in *Smith et al.* [2013]). We evaluated this uncertainty by
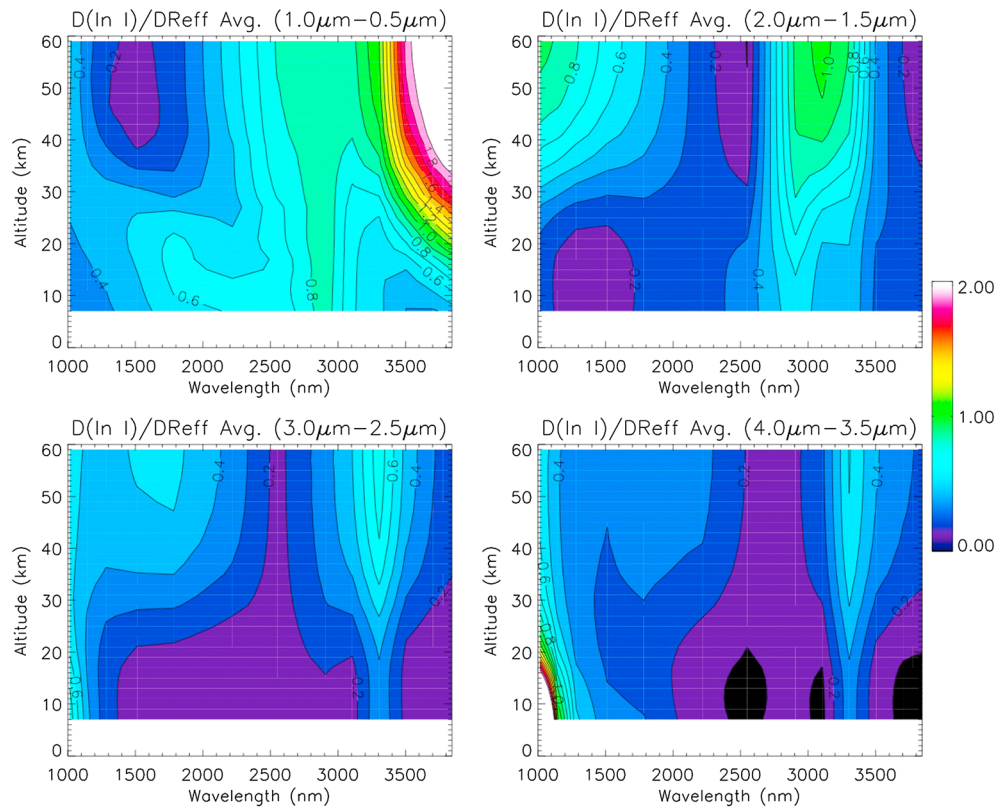
Figure 5. $\frac{d(\ln I)}{dr_{eff}}$ of CRISM observations over the indicated intervals in water ice effective radius in units of μm^{-1} as a function of wavelength and altitude. Larger numbers indicate greater sensitivity to water ice effective radius.

calculating the difference between the observed and computed radiance for the observations used in the study and determining the mean difference and standard deviation between these values (in terms of I/F). We then conducted a Monte Carlo test of our retrievals by adding random radiance (within ±3 standard deviations of the mean difference between observed and computed radiances for all observations) to each wavelength channel of the observed radiance and rerunning the retrieval algorithm. The resulting aerosol particle effective radii were consistent to within 0.05 μm (in absolute terms) of the initially retrieved aerosol particle effective radii.

The last source of uncertainty we examined is the correlated noise consisting of the uncertainty derived from correlated errors in the observed spectrum across wavelengths. To evaluate this uncertainty, we calculated the difference between the observed and computed radiance at all wavelengths for each of the 410 CRISM observations. We term this vector the "difference spectrum." To evaluate this source of uncertainty, a random difference spectrum was added to the observed radiance of a particular retrieval and the retrieval was redone. As before, we conducted Monte Carlo tests using these difference spectra to determine the uncertainty in our retrieved aerosol particle effective radius. The mean uncertainty in the retrieved aerosol particle effective radius in these scenarios was approximately 0.1 μm.

Using our forward radiance model, we can directly model the sensitivity of the CRISM retrieval to aerosol effective radius. For a specified effective radius, we use the forward model to compute the observed radiance, I, as a function of height and wavelength. We then numerically compute the derivative of radiance, I, as a function of effective radius, r_{eff}, $\frac{dI}{dr_{eff}}$. By dividing this quantity by radiance, I, we then calculate $\frac{d(\ln I)}{dr_{eff}}$. This is the fractional change in radiance from the forward model for a given change in aerosol effective radius.

In Figures 4 and 5, we show $\frac{d(\ln I)}{dr_{eff}}$ as a function of altitude and wavelength for given aerosol particle sizes of dust and water ice, respectively, in units of μm^{-1}. Large values of $\frac{d(\ln I)}{dr_{eff}}$ correspond to cases where the retrieval is more sensitive to changes in effective radius, and thus, uncertainties are lower. The retrieval is most
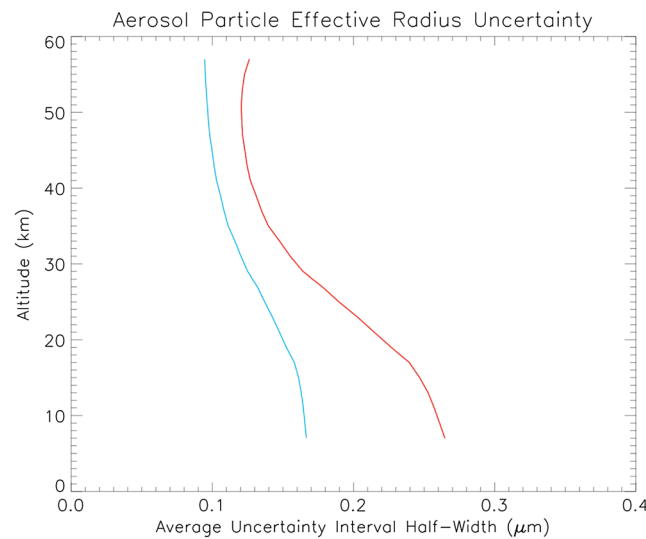
Figure 6. Average aerosol particle effective radius uncertainty interval half-width as a function of altitude over the 0.5–4.0 μm range for water ice (blue line) and 0.5–2.5 μm range for dust (red line).

sensitive to water ice near the 2800 nm water ice absorption feature, which is a prime reason for our selection of several wavelengths within this spectral range. These two figures also demonstrate that the retrieval is more sensitive to smaller aerosol particles. Given that there is much less radiance at high altitudes, in an absolute sense, the retrieval is more sensitive to small changes in aerosol effective radius at high altitudes, in general, than at lower altitudes. These two figures were produced assuming approximate "climatological" levels of aerosol optical depth to calculate retrieval sensitivity to aerosol particle size. We performed a test with aerosol optical depth tripled over that climatological level and the retrieval experiences only a very slight decrease in sensitivity to aerosol particle size (not shown).

Uncertainty in retrieved aerosol particle size can be estimated as $\frac{\sigma(I)}{I} / \frac{d(\ln I)}{dr_{eff}}$, where $\sigma(I)$ represents the standard deviation of the radiance and hence the numerator represents the fractional uncertainty in the observations. Following *Wolff et al.* [2009], we conservatively assume a 5% error in the radiometric accuracy of the observation. Using this formulation, Figure 6 shows our formal estimate of the average uncertainty in retrieved aerosol effective radius for dust and ice as a function of height. In the remaining figures showing retrieved aerosol effective radius, the error bars shown indicate the uncertainty for that particular effective radius and altitude.

By fitting for aerosol particle size directly, we have reduced one of the sources of error in aerosol mixing ratio retrieval discussed by *Smith et al.* [2013]. Still, to be conservative, we will use the same estimated mixing ratio uncertainty as *Smith et al.* [2013] (see their Figure 9), which is approximately 0.1 $\Delta\tau$/mb at most altitudes and slightly larger in the lowermost altitudes.

3. Analysis and Discussion

3.1. Aphelion Cloud Belt

The aphelion cloud belt (ACB) is an annually reoccurring feature of the current Martian climactic system. In northern spring, the northern polar cap begins to sublime and water vapor is transported southward toward the low latitudes. Vertical motion and the presence of ice nuclei (presumably dust) form frequent water ice clouds in the tropics and low-latitudes during late northern spring into the early portion of northern summer [e.g., *Smith*, 2004]. *Clancy et al.* [2003] found that the ACB generally consisted of larger cloud particles of 3.0–4.0 μm at lower altitudes and smaller 1.0–2.0 μm particles at higher altitudes.

Our results are generally consistent with those of *Clancy et al.* [2003]. Figure 7 shows water ice mixing ratio (Figure 7a) and retrieved water ice aerosol effective radius (or "particle size") (Figure 7b) averaged over the $L_s = 40°–110°$ period that spans the ACB season. The ACB is clearly seen in Figure 7a in the region of high ice mixing ratio centered near 35 km just north of the equator. At lower altitudes (below 30 km), the particle sizes are ≥2.0 μm, increasing to larger than 3.0 μm below 20 km. Above 30 km, water ice particle sizes decrease with height to 1 μm or smaller near 40 km. The strong sorting of particle size with height is shown again in Figure 8 at four latitude bands covering the densest portion of the ACB. At the base of the thickest clouds near 15 km, the ice particles are approximately 3.0 μm in size and there is a consistent steady decrease in particle size across the cloud from 15 to 40 km altitude. Our results also compare favorably to those of *Fedorova et al.* [2014] which analyzed the extreme northern edge of the ACB at 43°N at L_s ~55° and found cloud particles of 1.4 μm near 20 km decreasing to 1.1 μm at 37 km. While our results
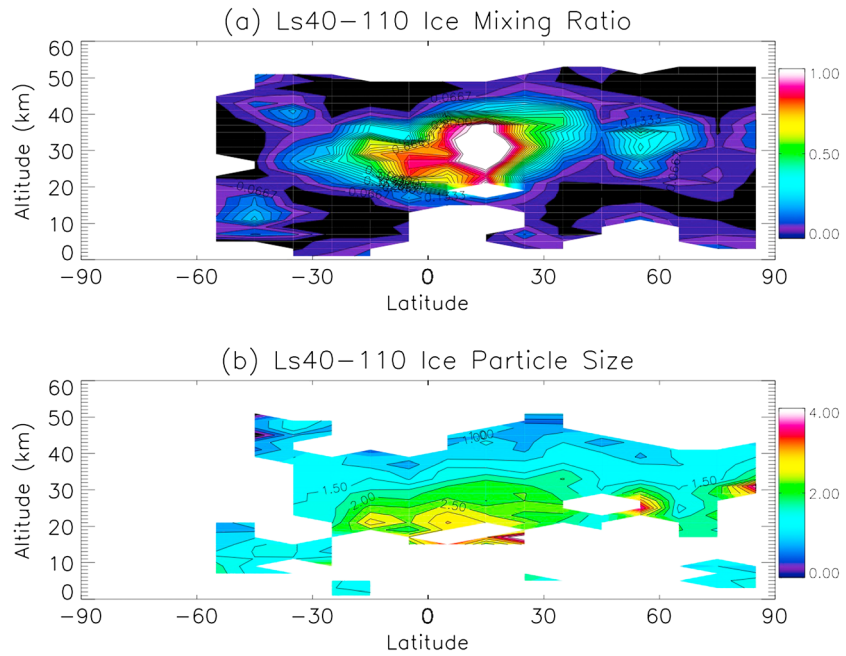
Figure 7. (a) The zonally averaged ice mixing ratio ($\Delta\tau$/mb at 2200 nm) during the $L_s = 40°$–110° period, covering the ACB season, as a function of height. (b) The corresponding retrieved ice effective radius (or "particle size") (μm).

suggest somewhat larger particles at 20 km in these latitudes, the higher altitude value is near our average retrieved value of approximately 1.25 μm.

Little differences are seen between the two observed longitudes in general, but slightly larger particles are favored at the lowermost altitudes near the equator in the Syrtis Major region relative to the Tharsis longitude
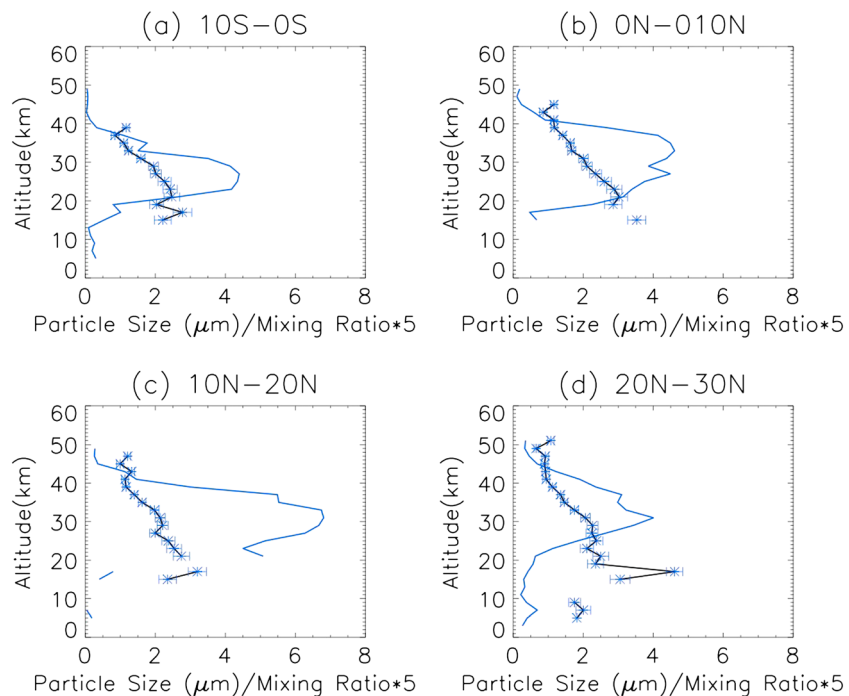
Figure 8. Water ice mixing ratio (solid blue lines, multiplied by 5 for clarity) and retrieved ice particle size (solid black line with blue asterisks) for (a) 10°S–0°S, (b) 0°N–10°N, (c) 10°N–20°N, and (d) 20°N–30°N for the $L_s = 40°$–110° period.
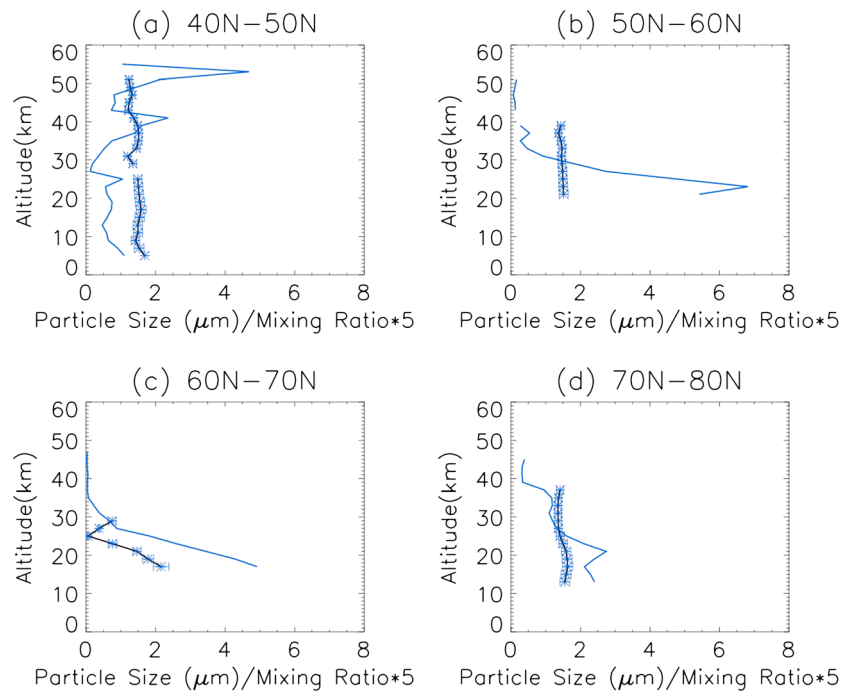
Figure 9. Water ice mixing ratio (solid blue lines, multiplied by 5 for clarity) and retrieved ice particle size (solid black line with blue asterisks) for (a) 40°N–50°N, (b) 50°N–60°N, (c) 60°N–70°N, and (d) 70°N–80°N for the $L_s = 330°$–360° period.

(not shown). In MY 32, particle sizes were modestly larger near the base of the ACB just north of the equator with particles larger than 3.0 μm up to 25 km (not shown).

This strong sorting of particle size as a function of altitude suggests (at least) two physical mechanisms for its presence. The first is that gravitational sedimentation efficiently settles larger particles to lower altitudes where eventually the ice is sublimated. At these altitudes and particle sizes, fall times are only a few sols [*Kahre et al.*, 2008]. Yet, this gravitational sedimentation signature is generally absent from our dust particle size retrievals (see section 3.3) or those of polar hood clouds (see section 3.2) implying that either vertical motions in the Martian atmosphere are very different with and without the presence of tropical water ice clouds or that another mechanism is producing this sorting with height.

Variability of microphysical parameters with height is another plausible explanation for the observed variation of particle size with height. In a simplified view to the complex problem of aerosol microphysics, there is presumably a balance through the atmospheric column between increased availability of water vapor allowing increasingly large particles and competition between greater numbers of available ice nuclei favoring smaller particles. Our results may suggest that at the cloud base the increased availability of water vapor dominates, resulting in larger particles, while at higher altitudes, this balance is reversed and smaller particles are the result. Possible transport of cloud particles through the atmospheric column (via updrafts or sedimentation) complicates this picture. Given the cold temperatures and small size of the particles (relative to terrestrial cirrus clouds), aggregation or clumping of particles is presumably a small or nonexistent factor.

3.2. Polar Hood Clouds

Water ice clouds fill and outline the Martian polar vortex as it develops each year in local winter from approximately 10 to 40 km altitude [*Benson et al.*, 2010, 2011]. Since CRISM relies on reflected sunlight to observe aerosols, observations of the polar hood clouds are limited. Yet, some consistent trends are present in retrieved water ice particle size between the polar hood clouds of both hemispheres. The clearest picture of the northern polar hood is obtained during the $L_s = 330°$–360° season and is shown in Figure 9. At latitudes poleward of 40°N, the water ice particle size is generally uniform with height at a value of 1.4–1.6 μm. Similar particle sizes are seen for the southern hemisphere polar hood during the $L_s = 0°$–30° season with slightly more variability with height (Figure 10). A handful of observations from the edge of the polar hood (40°–60°S)
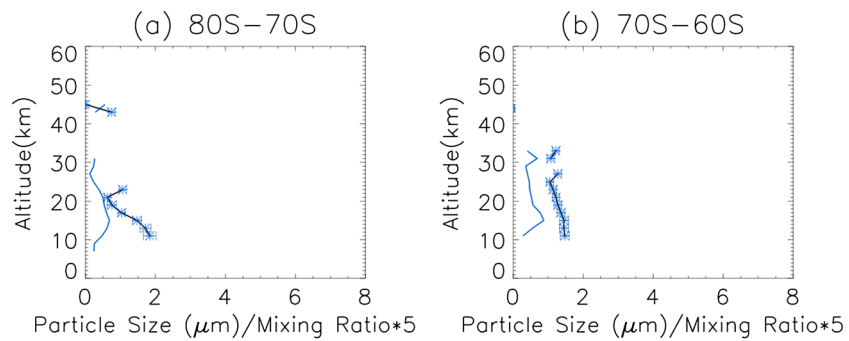
Figure 10. Water ice mixing ratio (solid blue lines, multiplied by 5 for clarity) and retrieved ice particle size (solid black line with blue asterisks) for (a) 80°S–70°S and (b) 70°S–60°S for the $L_s = 0°$–30° period.

later in the Martian year corroborate this trend with particle sizes again near 1.5 μm (not shown). *Fedorova et al.* [2014] also found water ice particle size to be fairly uniform with height at these latitudes but slightly smaller in size from 1.1 to 1.5 μm.

The stark differences in particle size and its variation with height between the polar hoods and the ACB reflect the differences between "Type 1" (1–2 μm and higher altitude clouds) and "Type 2" (3–4 μm clouds in the northern subtropical ACB) clouds identified by *Clancy et al.* [2003]. The uniformity of particle size between the two hemispheres and in the vertical column suggests consistent microphysical processes at work throughout the Martian high latitudes during local winter and in the vertical column that can replenish water ice particles at a rate faster than gravitational sedimentation can remove them.

3.3. Dust

One of the motivations for this study was to confirm or deny the possibility that small dust particle size is a key factor in maintaining the observed tropical detached dust layers over long periods of time [*Heavens et al.*, 2011; *Guzewich et al.*, 2013]. The mechanisms that supply dust to that altitude are as yet unknown, although several possibilities have been suggested in the literature [*Heavens et al.*, 2011; *Guzewich et al.*, 2013; *Spiga*
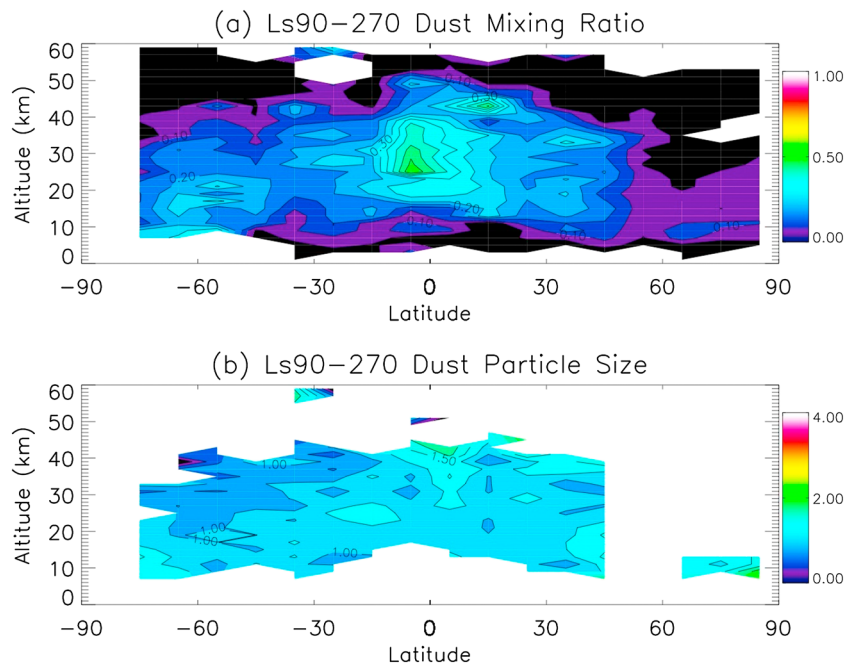

Figure 11. (a) The zonally averaged dust mixing ratio ($\Delta\tau$/mb at 2200 nm) during the $L_s = 90°$–270° period as a function of height. (b) The corresponding retrieved dust particle size (μm).
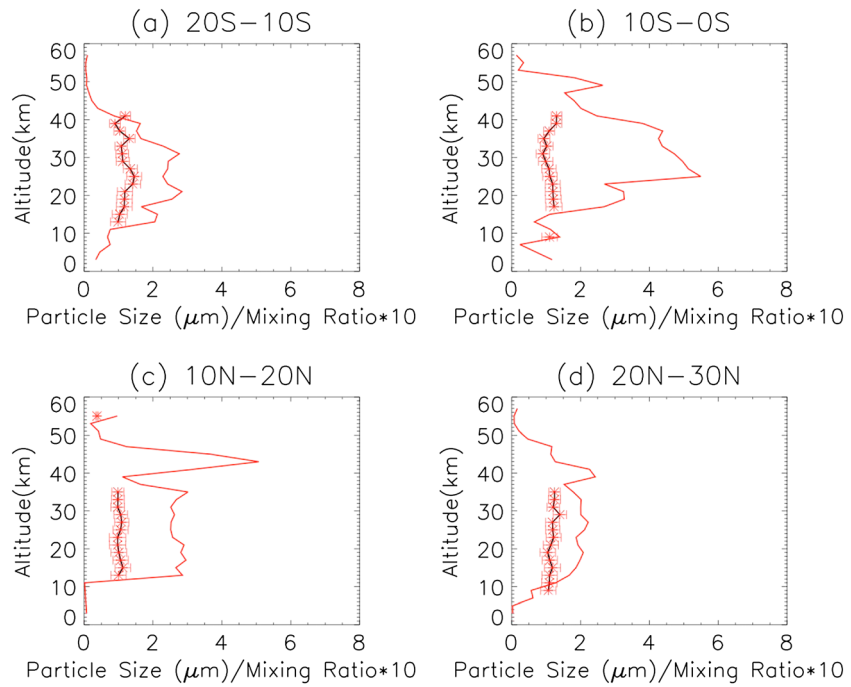
Figure 12. Dust mixing ratio (solid red lines, multiplied by 10 for clarity) and retrieved dust particle size (solid black line with red asterisks) for (a) 20°S–10°S, (b) 10°S–0°S, (c) 10°N–20°N, and (d) 20°N–30°N for the $L_s = 90°–270°$ period.
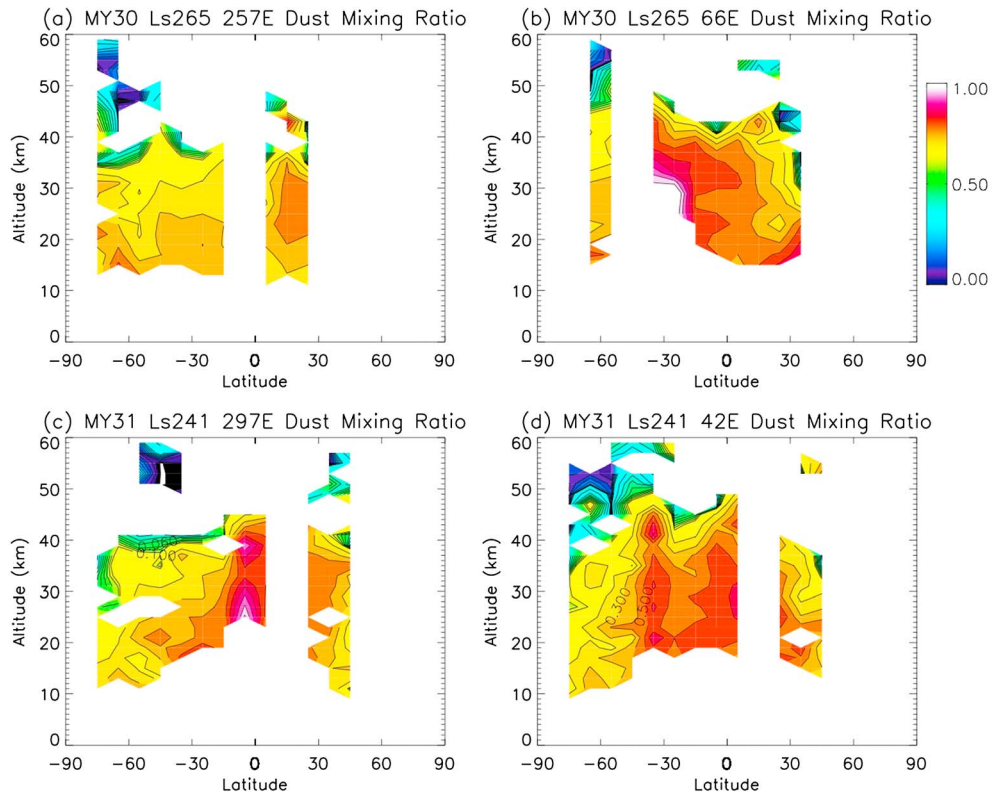
Figure 13. The zonally averaged dust mixing ratio ($\Delta\tau$/mb at 2200 nm) as a function of height during the (a) MY 30 $L_s = 265°$ MRO passes near 257°E, (b) MY 30 $L_s = 265°$ MRO passes near 66°E, (c) MY 31 $L_s = 241°$ MRO passes near 297°E, and (d) MY 31 $L_s = 241°$ MRO passes near 42°E.
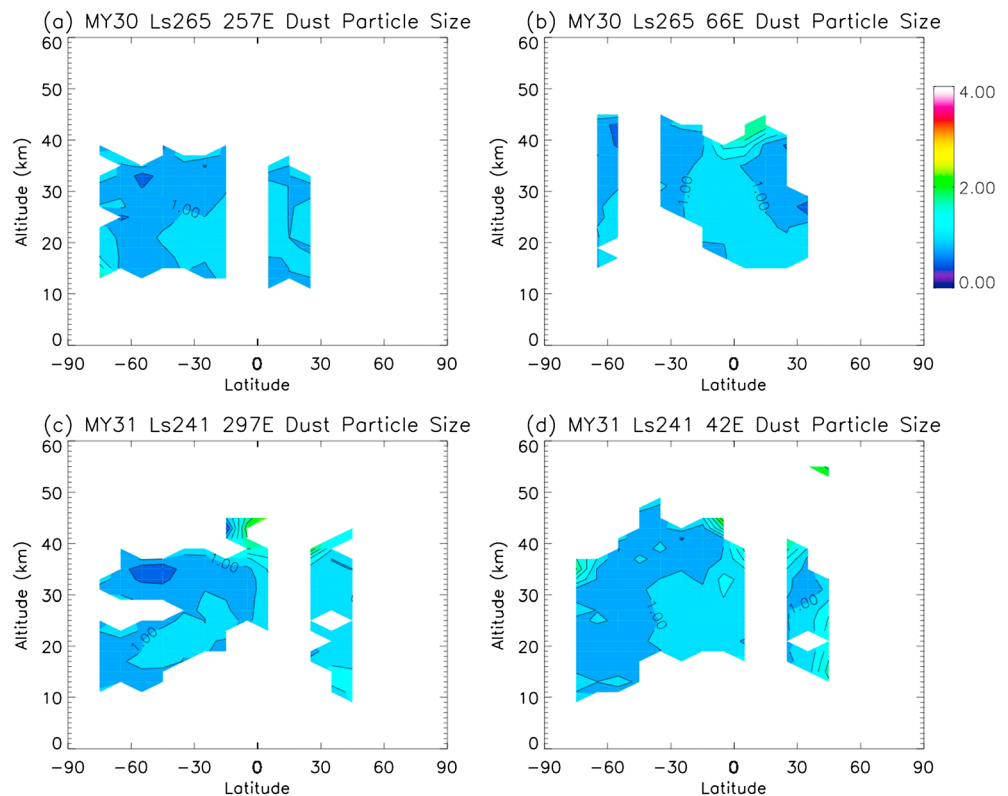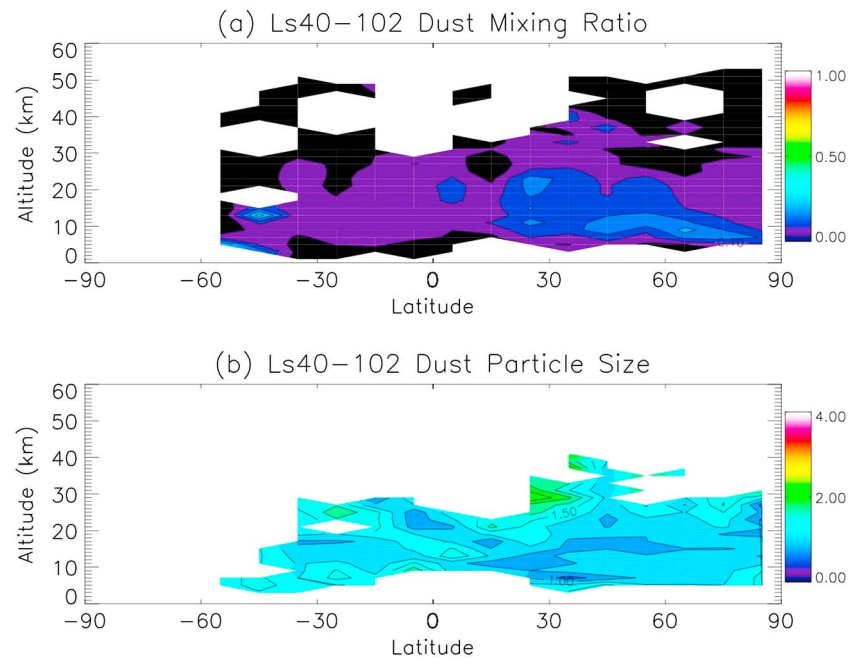
Figure 14. The retrieved dust particle sizes (μm) for the same CRISM observations as displayed in Figure 13.

et al., 2013]. If smaller particles were being supplied to these dust layers, then these resupply mechanisms would presumably not need to operate on a regular basis, and an infrequent supply of dust could be sufficient to maintain the dust layers throughout most of the Martian year.

We find that dust particle size is quite uniform in the tropics with an effective radius of approximately 1.0 μm, including in the detached dust layer at 20–30 km altitude (Figures 11 and 12). The tropical detached dust layer is clearly present in Figure 11a, but there is no suggestion of it being distinct in particle size from the rest of the lower and middle atmosphere (Figure 11b). Indeed, it is clear from Figures 11 and 12 that the dust particle size throughout the atmospheric column between the near-surface and ~40 km is consistently near 1.0 μm. The variation in particle size in the tropical detached dust layer between different Mars years or the two longitudes is on the order of ±0.1–0.2 μm, which is within our estimated uncertainties. SPICAM observations also have indicated a nearly uniform dust particle size with height at approximately 0.7–0.8 μm [*Fedorova et al.*, 2014].

The uniformity to a dust particle size of approximately 1.0 μm in the lower and middle atmosphere is generally valid outside of the tropics as well. Dust particle size is relatively invariant despite changing atmospheric dust loading and even within some small-to-regional scale dust storms. Figure 13 shows retrieved dust mixing ratios at nearly the same time period in MY 30 and MY 31 and covering two longitudes. The late southern spring season can exhibit widely varying atmospheric dust conditions [e.g., *Smith*, 2004], and this is exemplified in Figure 13 where the large differences between the two Martian years are clear. A regional dust storm is actively occurring in and around Hellas Basin in Figure 13b, with dust mixing ratios greater than unity at altitudes up to 30 km. Yet, despite that variability in total atmospheric dust loading between the two Martian years, and despite the variations between conditions in the different hemispheres within the same year, the dust particle size is always near 1.0 μm (Figure 14).

The consistency of dust particle size in the lower and middle atmosphere in our CRISM retrievals implies that this region of the atmosphere is well mixed on short timescales, at least during the later half to two thirds of the Martian year. The fall lifetimes of 1.0 μm dust particles at these altitudes is 2–20 sols [*Kahre et al.*, 2008], and thus, dust must be resupplied steadily from the surface and mixed uniformly through the column on timescales no longer than that period. Based on our work and that of *Fedorova et al.* [2014], the larger dust

Figure 15. (a) The zonally averaged dust mixing ratio ($\Delta\tau$/mb at 2200 nm) during the MY 31 $L_s = 40°–102°$ period as a function of height. (b) The corresponding retrieved dust particle size (μm).

particle sizes observed by previous column-integrated studies [e.g., *Wolff and Clancy*, 2003; *Wolff et al.*, 2006] are likely located in the lowest atmospheric scale height (i.e., the boundary layer). Given that dust mixing ratios are generally higher in the boundary layer, that larger particles require more force to loft to higher heights, and that larger particles have faster fall speeds, the observed limiting of dust particles larger than 1.5 μm to the lowest altitudes is consistent with previous studies.

The greatest departure from dust particle size of 1.0 μm in our retrievals is from early in MY 31. CRISM conducted a series of limb-viewing observations during MY 31 at $L_s = 41°$, $L_s = 62°$, and $L_s = 101°$. During this period, the average dust particle size observed is 1.3 μm. This period of the Martian year is known as one that is less dusty than later portions of the year, and this is confirmed in the CRISM retrievals (compare Figure 15a to Figure 11). Weather reports from the Mars Color Imager [*Malin et al.*, 2011, 2012a, 2012b] for this time period also report little dust storm activity. In Figure 15b, we show that the larger ($>1 \mu$m) dust particles are widespread in latitude during this period early in MY 31. Little differences in particle size are seen between different longitudes (not shown). In addition to larger dust particles being present, there is far greater variability of particle size in altitude during this time period relative to the other CRISM observations (e.g., Figures 11b and 12). No CRISM data are available for comparable times during MY 30, but some data are available at the same time in MY 32. Dust particle sizes in early MY 32 are slightly less than in early MY 31 but generally within the error bars and again larger than the 1.0 μm particles that predominate most of the year (not shown). The predominance of larger dust particles during the early portion of the year relative to later parts of the year (i.e., the canonical "dust storm season" surrounding perihelion) is counterintuitive given that the atmospheric circulation is more vigorous later in the year, which should allow for stronger winds that have a higher likelihood of lofting larger dust particles.

4. Conclusions

We have conducted retrievals of dust and water ice aerosol effective radius (or "particle size") for approximately 410 limb-viewing geometry observations of the Martian atmosphere by CRISM, enabling us to determine the variation of particle size with altitude. These observations have been conducted periodically during MY 30-MY 32 and generally include pole-to-pole limb scans at two longitudes corresponding to Syrtis Major/Hellas Basin and the Tharsis Montes. Our attention in this paper has been focused on the aphelion cloud belt, polar hood clouds, and dust.

Water ice particles in the aphelion cloud belt are strongly sorted in size by altitude, with a 3.0 μm effective radius for particles near the base of the cloud, decreasing to near 1.0 μm at the top of the cloud. This result is consistent with that of *Clancy et al.* [2003] who found the aphelion cloud belt to be composed of "Type 1" clouds with smaller particles at higher altitudes and "Type 2" clouds with larger particles at lower altitudes.

The polar hood clouds in both hemispheres have greater uniformity in particle size as a function of altitude, with a consistent effective radius of approximately 1.5 μm within the clouds. This is true even when the dual-layer structure of the polar hood clouds [*Benson et al.*, 2010, 2011] is present (e.g., Figures 10a and 10d).

One of the motivations of this work was to confirm or deny the idea that small dust particle size could serve as a mechanism to maintain the detached tropical dust layers identified by *Heavens et al.* [2011] and *Guzewich et al.*, 2013]. We show that dust particles within the 20–30 km detached dust layer have predominantly the same effective radii as the remainder of the atmosphere below 40 km altitude with an effective radius near 1.0 μm. In fact, the effective radius of dust particles is remarkably uniform in the CRISM retrievals with retrieved values near 1.0 μm for most times of the year and at all latitudes. This is true during the dust storm season surrounding perihelion, even with widely varying atmospheric dust loading between MY 30 and MY 31. The only notable departure to this is in early MY 31, when the average dust particle effective radius throughout the atmosphere was approximately 1.3 μm and greater variation in particle size with height was observed. Our work suggests that previous column integrated studies of dust particle size that found effective radii of ~1.5 μm [e.g., *Wolff and Clancy*, 2003; *Wolff et al.*, 2006] are likely primarily retrieving the dust particle size in the lowest scale height of the atmosphere, to which the CRISM retrievals are generally insensitive.

As dust is a nearly omnipresent aerosol in the Martian atmosphere, the general uniformity of particle size suggests that the lower atmosphere (~10–40 km altitude) is well-mixed on timescales of 2–20 sols, which is shorter than the settling rate of 1.0 μm dust particles at these altitudes. There is no prevalent indication of gravitational sedimentation producing a sorting of dust particle size with height. A sedimentation-like sorting of ice particle size with height is present in the aphelion cloud belt, however. If that feature is truly caused by gravitational sedimentation, then the mixing of the atmosphere that appears predominant below the clouds must weaken within the cloud to allow for particle size sorting by height within the clouds. It is also possible that microphysical parameters change over the altitude span of the cloud, leading to creation of different ice particle sizes at different heights. The CRISM observations are unable to distinguish between these scenarios. In either case, the microphysical environment of the polar hood clouds is clearly different from that of the tropical aphelion cloud belt, since the polar hood clouds exhibit a nearly uniform ice particle size with height, more similar to the pattern exhibited by dust particles. We expect that these results will help constrain and inform the microphysical parameterizations used in atmospheric general circulation models. For example, the presence of larger than expected 1.0 μm dust particles at higher altitudes may make clouds form more easily in microphysical parameterizations then they would on smaller dust particles. A more representative distribution of aerosol particle size with height, and thus the optical depth profile as a function of height, will allow models to refine the way aerosols are treated in their radiation codes.

References

Benson, J. L., D. M. Kass, A. Kleinböhl, D. J. McCleese, J. T. Schofield, and F. W. Taylor (2010), Mars' south polar hood as observed by the Mars Climate Sounder, *J. Geophys. Res.*, 115, E12015, doi:10.1029/2009JE003554.

Benson, J. L., D. M. Kass, and A. Kleinböhl (2011), Mars' north polar hood as observed by the Mars Climate Sounder, *J. Geophys. Res.*, 116, E03008, doi:10.1029/2010JE003693.

Clancy, R. T., and S. W. Lee (1991), A new look at dust and clouds in the Mars atmosphere: Analysis of emission-phase-function sequences from global Viking IRTM observations, *Icarus*, 93, 135–158.

Clancy, R. T., S. W. Lee, G. R. Gladstone, W. McMillan, and T. Roush (1995), A new model for Mars atmospheric dust based upon analysis of ultraviolet through infrared observations from Mariner 9, Viking, and Phobos, *J. Geophys. Res.*, 100, 5251–5263, doi:10.1029/94JE01885.

Clancy, R. T., M. J. Wolff, and P. R. Christensen (2003), Mars aerosol studies with the MGS-TES emission phase function observations: Optical depths, particle sizes, and ice cloud types versus latitude and solar longitude, *J. Geophys. Res.*, 108, doi:10.1029/2003JE002058.

Clancy, R. T., M. J. Wolff, B. A. Whitney, B. A. Cantor, M. D. Smith, and T. H. McConnochie (2010), Extension of atmospheric dust loading to high altitudes during the 2001 Mars dust storm: MGS TES limb observations, *Icarus*, 207, 98–109.

Deirmendjian, D. (1964), Scattering and polarization of water clouds and hazes in the visible and infrared, *Appl. Opt.*, 3(2), 187–196.

Fedorova, A. A., O. I. Korablev, J.-L. Bertaux, A. V. Rodin, F. Montmessin, D. A. Belyaev, and A. Reberac (2009), Solar infrared occultations by the SPICAM experiment on Mars Express: Simultaneous observations of H_2O, CO_2 and aerosol vertical distribution, *Icarus*, 200, doi:10.1016/j.icarus.2008.11.006.

Fedorova, A. A., F. Montmessin, A. V. Rodin, O. I. Korablev, A. Määttänen, L. Maltagliati, and J.-L. Bertaux (2014), Evidence for a bimodal size distribution for the suspended aerosol particles on Mars, *Icarus*, 231, doi:10.1016/j.icarus.2013.12.015.

Goody, R. M., and Y. L. Yung (1989), *Atmospheric Radiation: Theoretical Basis*, Oxford Univ. Press, New York.

Guzewich, S. D., E. R. Talaat, A. D. Toigo, D. W. Waugh, and T. H. McConnochie (2013), High-altitude dust layers on Mars: Observations with the thermal emission spectrometer, *J. Geophys. Res. Planets*, *118*, 1177–1194, doi:10.1002/jgre.20076.

Heavens, N. G., J. L. Benson, D. M. Kass, A. Kleinböhl, W. A. Abdou, D. J. McCleese, M. I. Richardson, J. T. Schofield, J. H. Shirley, and P. M. Wolkenberg (2010), Water ice clouds over the Martian tropics during northern summer, *Geophys. Res. Lett.*, *37*, L18202, doi:10.1029/2010GL044610.

Heavens, N. G., M. I. Richardson, A. Kleinböhl, D. M. Kass, D. J. McCleese, W. Abdou, J. L. Benson, J. T. Schofield, J. H. Shirley, and P. M. Wolkenberg (2011), Vertical distribution of dust in the Martian atmosphere during northern spring and summer: High-altitude tropical dust maximum at northern summer solstice, *J. Geophys. Res.*, *116*, E01007, doi:10.1029/2010JE003692.

Kahre, M. A., J. R. Murphy, and R. M. Haberle (2006), Modeling the Martian dust cycle and surface dust reservoirs with the NASA Ames general circulation model, *J. Geophys. Res.*, *111*, E06008, doi:10.1029/2005JE002588.

Kahre, M. A., J. L. Hollingsworth, R. M. Haberle, and J. R. Murphy (2008), Investigations of the variability of dust particle sizes in the Martian atmosphere using the NASA Ames General Circulation Model, *Icarus*, *195*, 576–597, doi:10.1016/j.icarus.2008.01.023.

Määttänen, A., C. Listowski, F. Montmessin, L. Maltagliati, A. Joly, A. Reberac, and J.-L. Bertaux (2013), A complete climatology of the aerosol vertical distribution on Mars from MEx/ SPICAM UV solar occultations, *Icarus*, *223*, 892–941, doi:10.1016/j.icarus.2012.12.001.

Madeleine, J.-B., F. Forget, E. Millour, T. Navarro, and A. Spiga (2012), The influence of radiatively active water ice clouds on the Martian climate, *Geophys. Res. Lett.*, *39*, L23202, doi:10.1029/2012GL053564.

Malin, M. C., B. A. Cantor, T. N. Harrison, D. E. Shean and M. R. Kennedy (2011), MRO MARCI Weather Report for the week of 12 December 2011 – 18 December 2011, Malin Space Science Systems Captioned Image Release, MSSS-202, http://www.msss.com/msss_images/2011/12/21/.

Malin, M. C., B. A. Cantor, M. R. Kennedy, D. E. Shean and T. N. Harrison (2012a), MRO MARCI Weather Report for the week of 23 January 2012 – 29 January 2012, Malin Space Science Systems Captioned Image Release, MSSS-208, http://www.msss.com/msss_images/2012/02/01/.

Malin, M. C., B. A. Cantor, T. N. Harrison, D. E. Shean and M. R. Kennedy (2012b), MRO MARCI Weather Report for the week of 23 April 2012 – 29 April 2012, Malin Space Science Systems Captioned Image Release, MSSS-222, http://www.msss.com/msss_images/2012/05/02/.

Mishchenko, M. I., J. W. Hovenier, and L. D. Travis (Eds.) (2000), *Light Scattering by Nonspherical Particles: Theory, Measurements, and Applications*, Academic Press, San Diego, Calif.

Montmessin, F., et al. (2006), Subvisible CO_2 ice clouds detected in the mesosphere of Mars, *Icarus*, *183*, 403–410, doi:10.1016/j.icarus.2006.03.015.

Murchie, S., et al. (2007), Compact Reconnaissance Imaging Spectrometer for Mars (CRISM) on Mars Reconnaissance Orbiter (MRO), *J. Geophys. Res.*, *112*, E05S03, doi:10.1029/2006JE002682.

Pollack, J. B., M. E. Ockert-Bell, and M. K. Shepard (1995), Viking Lander image analysis of Martian atmospheric dust, *J. Geophys. Res.*, *100*, 5235–5250, doi:10.1029/94JE02640.

Press, W. H., S. A. Teukolsky, W. T. Vetterling, and B. P. Flannery (1992), *Numerical Recipes in Fortran 77: The Art of Scientific Computing*, Cambridge Univ. Press, Cambridge, U. K.

Rannou, P., S. Perrier, J.-L. Bertaux, F. Montmessin, O. Korablev, and A. Rébérac (2006), Dust and cloud detection at the Mars limb with UV scattered sunlight with SPICAM, *J. Geophys. Res.*, *111*, doi:10.1029/2006HE002693.

Smith, M. D. (2004), Interannual variability in TES atmospheric observations of Mars during 1999–2003, *Icarus*, *167*, 148–165.

Smith, M. D., M. J. Wolff, R. T. Clancy, A. Kleinböhl, and S. L. Murchie (2013), Vertical distribution of dust and water ice aerosols from CRISM limb-geometry observations, *J. Geophys. Res. Planets*, *118*, 321–334, doi:10.1002/jgre.20047.

Spiga, A., J. Faure, J.-B. Madeleine, A. Määttänen, and F. Forget (2013), Rocket dust storms and detached dust layers in the Martian atmosphere, *J. Geophys. Res. Planets*, *118*, 746–767, doi:10.1002/jgre.20046.

Thomas, G. E., and K. Stamnes (1999), *Radiative Transfer in the Atmosphere and Ocean*, Cambridge Univ. Press, Cambridge, U. K.

Toigo, A. D., M. D. Smith, F. P. Seelos, and S. L. Murchie (2013), High spatial and temporal resolution sampling of Martian gas abundances from CRISM spectra, *J. Geophys. Res. Planets*, *118*, 89–104, doi:10.1029/2012JE004147.

Toon, O. B., J. B. Pollack, and C. Sagan (1977), Physical properties of the particles composing the Martian dust storm of 1971, *Icarus*, *30*, 663–696.

Warren, S. (1984), Optical constants of ice from the ultraviolet to the microwave, *Appl. Opt.*, *23*, 1206–1225.

Wilson R. J. and S. D. Guzewich (2014), Influence of water ice clouds on nighttime tropical temperature structure as seen by the Mars Climate Sounder, *Geophys. Res. Lett.*, *41*, 3375–3381, doi:10.1002/2014GL060086.

Wiscombe, W. J. (1996), Mie scattering calculations: Advances in technique and fast, vector speed computer codes, NCAR/TN-140 + STR, Natl. Cent. Atmos. Res., Boulder, Colo.

Wolff, M. J., and R. T. Clancy (2003), Constraints on the size of Martian aerosols from thermal emission spectrometer observations, *J. Geophys. Res.*, *108*(E9), 5097, doi:10.1029/2003JE002057.

Wolff, M. J., et al. (2006), Constraints on dust aerosols from the mars exploration rovers using MGS overflights and Mini-TES, *J. Geophys. Res.*, *111*, E12S17, doi:10.1029/2006JE002786.

Wolff, M. J., R. T. Clancy, M. D. Smith, R. Arvidson, M. Kahre, F. Seelos IV, and R. V. Morris (2009), Wavelength dependence of dust aerosol single scattering albedo as observed by CRISM, *J. Geophys. Res.*, *114*, E00D04, doi:10.1029/2009JE003350.